ACCEPTED VERSION

Tingyuan Yin, Ching-Tai Ng, Andrei Kotousov
Damage detection of ultra-high-performance fibre-reinforced concrete using a harmonic wave modulation technique

---

PERMISSIONS

https://www.elsevier.com/about/policies/sharing

Accepted Manuscript

Authors can share their accepted manuscript:

24 Month Embargo

After the embargo period

- via non-commercial hosting platforms such as their institutional repository
- via commercial sites with which Elsevier has an agreement

In all cases accepted manuscripts should:

- link to the formal publication via its DOI
- bear a CC-BY-NC-ND license – this is easy to do
- if aggregated with other manuscripts, for example in a repository or other site, be shared in alignment with our hosting policy
- not be added to or enhanced in any way to appear more like, or to substitute for, the published journal article

19 December 2023

---

http://hdl.handle.net/2440/135272

Journal article:

Tingyuan Yin, Ching Tai Ng, Andrei Kotousov. (2021). Damage detection of ultra-high-performance fibre-reinforced concrete using a harmonic wave modulation technique. Construction and Building Materials, 313:125306.

Damage detection of ultra-high-performance fibre-reinforced concrete using a harmonic wave modulation technique

Tingyuan Yin[1], Ching-Tai Ng[1,*], Andrei Kotousov[2]

[1] School of Civil, Environmental & Mining Engineering, The University of Adelaide, SA 5005, Australia

[2] School of Mechanical Engineering, The University of Adelaide, SA 5005, Australia

Abstract

In this paper, a damage detection technique, named cross-modulated vibro-acoustic (CMVA) technique, is proposed to detect damages induced by flexural loading in ultra-high-performance fibre-reinforced concrete (UHP-FRC) material. Different from conventional vibro-acoustic methods, the pump wave of the proposed CMVA technique is modulated by two low-frequency waves to address limitations of pump wave generator on excitation frequency. The proposed technique has lower power consumption and high sensitivity to micro-damages. In this study, a mechanical model of contact nonlinearity at interfaces is developed to establish the nonlinear parameter D_α for the proposed CMVA technique in describing various flexural damage levels. The conventional resonant frequency (RF) test based on ASTM C215-02, is conducted to compare with the results of the proposed CMVA technique. This study presents the application of the proposed CMVA technique to monitor the damage evolution the UHP-FRC structure. The experimental results show that the sensitivity of D_α to early-stage damages and material degradation is much higher than the conventional measurement of RF test. Therefore, the proposed CMVA technique is an accurate and reliable technique to monitor progressive damages in structures.

---

[*] Corresponding author: alex.ng@adelaide.edu.au

1. Introduction

Concrete is one of the most commonly used materials in civil infrastructures and buildings throughout the world. To improve its strength, toughness and durability of concrete, researchers have developed different approaches to enhance its engineering properties so that its usages in construction can be further extended. Fibre-reinforced concrete is one of the potential materials to meet the high demands of modern civil engineering construction. The buildings and infrastructures made by this material can be subjected to extreme loads or conditions, e.g. earthquakes, strong winds and fires, or long-term attacks, e.g. freeze-thaw deterioration, chemical erosion and alkali-aggregate reaction [1, 2] and damage or aging may happen on the structures. Therefore, non-destructive evaluation (NDE) techniques for detecting and evaluating damages after short-term overloads and structural health monitoring (SHM) techniques for monitoring accumulated damages under long-term attacks are of great importance in civil engineering structures.

Acoustic and ultrasonic techniques have been applied to ensure the safety and integrity of concrete in the literature because of their simple operation procedure, less labour cost and relative low-priced instrumentation compared to other advanced NDT techniques. Linear features of acoustic and ultrasonic techniques, such as velocity [3-6] and amplitude attenuation [7, 8] of the acoustic and ultrasonic waves, have been widely used to assess various damages in concrete. However, it has been demonstrated that these linear features of acoustic and ultrasonic techniques are not sensitive enough to provide early-stage detection of damage for concrete structures. It is because these techniques are based on linear constitutive relationship, by which it assumes damage in medium only affect elastic modulus. But the effect of the decrease in elastic modulus is insensitive even when macro-crack is evident.

1.1 Vibro-acoustic Techniques

Recently, acoustic and ultrasonic techniques based on nonlinear features, such as higher harmonics, frequency shift and sidebands, have attracted significant research interests in the area of NDE and SHM [9-12]. It has been demonstrated that these nonlinear features are attractive for damage detection because they are not only susceptible to the formation of macro-cracks but also the initiation of micro-cracks at the early damage stage [13-16]. Acoustic and ultrasonic signals exhibit nonlinear features when the waves travel in a nonlinear medium. The growth of discontinuity in the materials is reflected by the increase of amplitudes of the

nonlinear components. Kim *et al*. [17], Chen *et al*. [18]. and Mohseni *et al*. [19, 20] investigated higher harmonic generation performance due to the discontinuity of materials for damage detection. Besides, Leśnicki *et al*. [21], Chen *et al*. [22] and Carrión *et al*. [23] employed the impact excitation as the source of the signal and analysed resonance frequency shift to characterize alkali-silica reaction damage, sulphate attack and freeze-thaw cycle damage, and thermal damage, respectively. The other application of nonlinear feature to characterize damage is sideband. Many theoretical and experimental studies focused on sideband have been carried out in the literature, but they mainly focused on conventional vibro-acoustic technique.

There are two primary vibro-acoustic technique approaches the impact-modulation (IM) method and the vibro-modulation (VM) method. The IM method uses impact excitation to induce resonance vibration modes of structures, while the VM method uses harmonic excitation in the damage detection [24]. Chen *et al*. [25-27] investigated the evolution of concrete damage caused by mechanical load and chemical attack using the IM and the VM method. Also, they developed a non-contact VM method to assess thermal damage of cement-based materials. However, accurate determination of sideband frequencies through the IM method is difficult for concrete or concrete-related materials because the resonance modes of structures are usually not well separated. The sidebands of resonance frequencies are easily masked by noise or the aliasing effect in signal processing. Furthermore, in the VM method, low-frequency signals are generally generated by electromagnetic shaker, and it causes a considerable burden for exciter to generate significant energy excitation at low-frequency. Also, the large oscillation caused by low-frequency signals will affect coupling conditions between transducers and structures.

1.2 Cross-modulated Vibro-acoustic Techniques

Zaitsev *et al*. carried out an experiment on a glass rod with thermally produced cracks to demonstrate the high sensitivity of the cross-modulated vibro-acoustic (CMVA) technique [28]. Tournat *et al*. conducted a series of experimental studies in a granular medium composed of glass beads to observe the cross-modulation effect. The results showed that sidebands are much more sensitive to weak perturbations of the medium [29]. In the study of Aymerich and Staszewski, the CMVA technique was applied to detect impact damage in composite laminates [30]. Trojniar *et al*. investigated fatigue cracks in the aluminium plate using the CMVA technique [31]. However, studies focused on the application of the CMVA technique on cement-based material have been very limited in the literature. The cement-based material is a more complex composite material compared with the glass and metal materials, and usually

used in the larger-size structures. Therefore, the phenomena in the cement-based material utilizing the CMVA technique is different to the glass and metal materials. In the aforementioned studies focused on CMVA techniques, only a single low frequency was transferred from the pump wave to the carrier wave, and nonlinear parameter was only related to this transferred lower frequency and carrier frequency.

This paper proposes an improved CMVA technique to address IM and VM limitations. Similar to the conventional VM method, the proposed CMVA technique relies on the interactions between a high-frequency carrier wave and a low-frequency harmonic vibration in the medium. Sidebands can be observed when the medium is discontinuous. The difference between the CMVA technique and the conventional VM method is the low-frequency harmonic excitation. The VM method employs a single-frequency continuous sine wave as the low-frequency excitation signal, whereas in the proposed CMVA technique, the low-frequency excitation signal is modulated by two excitation frequencies (f_{L1} and f_{L2}, f_{L1} is the resonance frequency and $f_{L1} < f_{L2}$). By employing modulated low-frequency pump signal, the proposed CMVA technique has the following advantages:

- Address the instrumental bottleneck frequency range, particularly for the ultra-low and/or low frequency. For full-scale structures, especially for civil engineering structures, the resonance frequencies are relatively low (in the order of Hertz). A modulated low-frequency pump signal, which contains not only resonance frequency (f_{L1}) but also a higher frequency excitation (f_{L2}), is used to induce such low-frequency resonance of these structures. Hence, actuators only need to transmit signal at f_{L2} instead of ultra-low or low frequency f_{L1}, meanwhile the sidebands related to f_{L1} can still be induced and measured.

- The required power of the actuator in generating a large enough magnitude of modulated pump signal is significantly less than that of using a single resonance frequency signal. This means the proposed CMVA technique is more energy-efficient and practical in an actual application in civil engineering structures.

- Minimise attenuation of wave propagation while maintaining the sensitivity to micro-damages. The modulated pump signal at low frequency (f_{L1} and f_{L2}) could reduce the energy attenuation. But the wavelength at low frequency is large, and hence, it is insensitive to micro-damages. Although the high-frequency signal with a smaller wavelength can characterize small defects and cracks, the wave attenuates rapidly in the propagation. The proposed CMVA technique combines a carrier signal at high-frequency

(f_H) and a modulated low-frequency pump wave $(f_{L1}$ and $f_{L2})$ to enhance the applicability and sensitivity for NDT and SHM of civil engineering structures.

One of the objectives of this paper is to quantitatively assess the accumulation damage in ultra-high-performance fibre-reinforced concrete (UHP-FRC) materials using the improved CMVA technique. Particularly, this study is expected to demonstrate both frequencies of pump wave $(f_{L1}$ and $f_{L2})$ are transferred to the carrier wave (f_H) when there are cracks in the cement-based material. The other objective is to develop the theoretical framework and derive the equations for the improved CMVA technique. In addition, a nonlinear parameter D_α is then defined to provide the relationship between the amplitudes of sidebands and amplitudes of other frequency components, which allow evaluation of the damage. To validate and evaluate the performance of the improved CMVA technique, the results are compared with a conventional damage evaluation technique based on ASTM C215-02 [32]. The experimental results demonstrate that the nonlinear parameter is closely related to the damage and can be used as a sensitive and reliable indicator to detect and monitor structural damage in UHP-FRC.

2. Proposed Cross-modulated Vibro-acoustic Technique

Assuming that there is a gap distance d due to defects or flexural loading between two rough surfaces, three incident longitudinal waves normally propagate to the interface, at which they separate into transmitted waves and reflected waves as shown in Fig.1. The displacement field between two rough interfaces caused by the wave interaction can be written as

$$u(x,t) = \begin{cases} u_I(x - ct) + u_R(x + ct), & x < 0 \\ u_T(x - ct), & x > 0 \end{cases} \qquad (1)$$

where c is the incident longitudinal wave speed, x is taken along the wave propagation direction. $u_I(x - ct)$, $u_R(x + ct)$ and $u_T(x - ct)$ are displacement of incident wave, reflected wave and transmitted wave, respectively.
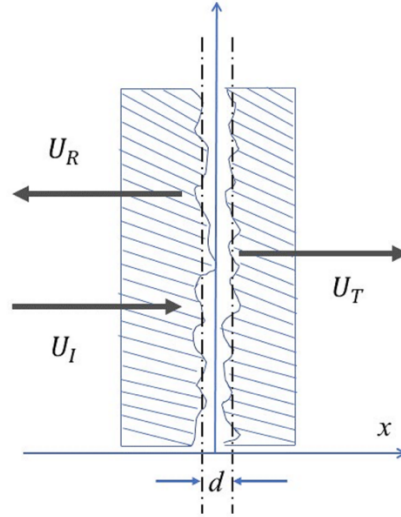
Fig.1 Longitudinal waves propagate through two rough interfaces

The incident wave leads to a dynamic opening-closing displacement on the rough interface and applying $u_I = A_1 cos[(\omega_1/c)(x - ct)] + A_2 cos[(\omega_2/c)(x - ct)] + A_3 cos[(\omega_3/c)(x - ct)]$, where A is the amplitude of wave and ω is the angular frequency, we have

$$\frac{d\xi(t)}{dt} = 2\sum_{i=1}^{3} A_i\omega_i sin\omega_i t - \frac{2K_1}{\rho c}\xi(t) + \frac{2K_2}{\rho c}\xi(t)^2 \tag{2}$$

where $\xi(t) = \Delta d$, K_1 and K_2 are the first and second-order terms of stiffness, respectively. ρ is the density of the medium, and c is the velocity of the wave propagating in the medium. By solving Eq.(3), the linear solution $\xi_1(t)$ is found,

$$\xi_1(t) = \sum_{i=1}^{3} \frac{2A_i c\rho\omega_i}{\sqrt{4k_1^2 + c^2\rho^2\omega_i^2}} sin(\omega_i t - \theta_i) \tag{3}$$

$$cos\theta_i = \frac{2k_1}{\sqrt{4k_1^2 + c^2\rho^2\omega_i^2}}, \qquad sin\theta_i = \frac{c\rho\omega_i}{\sqrt{4k_1^2 + c^2\rho^2\omega_i^2}} \tag{4}$$

Thus, we have a nonlinear solution $\xi_2(t)$ including (i) DC component, (ii) second-order harmonics, (iii) difference-sidebands and (iv) sum-sidebands, respectively as follows:

(i) DC component: this part does not contain any trigonometric functions.

$$2\frac{K_2}{K_1}\sum_{i=1}^{3} \frac{A_i^2 c^2\rho^2\omega_i^2}{4k_1^2 + c^2\rho^2\omega_i^2} \tag{5a}$$

(ii) Second order harmonics:

$$\sum_{i=1}^{3} \frac{2k_2 A_i^2 c^2 \rho^2 \omega_i^2}{\sqrt{k_1^2 + c^2\rho^2\omega_i^2}\,(4k_1^2 + c^2\rho^2\omega_i^2)} cos\,(2\omega_i t - 2\theta_i - \xi_i) \tag{5b}$$

$$cos\xi_i = \frac{k_1}{\sqrt{k_1^2 + c^2\rho^2\omega_i^2}}, \qquad sin\xi_i = \frac{c\rho\omega_i}{\sqrt{k_1^2 + c^2\rho^2\omega_i^2}} \tag{5c}$$

(iii) Difference-sidebands: They are difference-sidebands with difference frequencies of $(\omega_1 - \omega_2)$, $(\omega_1 - \omega_3)$ and $(\omega_2 - \omega_3)$.

$$\frac{-8k_2 A_1 A_2 c^2 \rho^2 \omega_1 \omega_2}{\sqrt{4k_1^2 + c^2\rho^2\omega_1^2}\sqrt{4k_1^2 + c^2\rho^2\omega_2^2}\sqrt{4k_1^2 + c^2\rho^2(\omega_1-\omega_2)^2}} cos[(\omega_1 - \omega_2)t - (\theta_1 - \theta_2) - \delta_1] -$$

$$\frac{8k_2 A_1 A_3 c^2 \rho^2 \omega_1 \omega_3}{\sqrt{4k_1^2 + c^2\rho^2\omega_1^2}\sqrt{4k_1^2 + c^2\rho^2\omega_3^2}\sqrt{4k_1^2 + c^2\rho^2(\omega_1-\omega_3)^2}} cos[(\omega_1 - \omega_3)t - (\theta_1 - \theta_3) - \delta_2] -$$

$$\frac{8k_2 A_2 A_3 c^2 \rho^2 \omega_2 \omega_3}{\sqrt{4k_1^2 + c^2\rho^2\omega_2^2}\sqrt{4k_1^2 + c^2\rho^2\omega_3^2}\sqrt{4k_1^2 + c^2\rho^2(\omega_2-\omega_3)^2}} cos[(\omega_2 - \omega_3)t - (\theta_2 - \theta_3) - \delta_3] \tag{5d}$$

$$cos\delta_1 = \frac{2k_1}{\sqrt{4k_1^2 + c^2\rho^2(\omega_1 - \omega_2)^2}}, \qquad sin\delta_1 = \frac{c\rho(\omega_1 - \omega_2)}{\sqrt{4k_1^2 + c^2\rho^2(\omega_1 - \omega_2)^2}}$$

$$cos\delta_2 = \frac{2k_1}{\sqrt{4k_1^2 + c^2\rho^2(\omega_1 - \omega_3)^2}}, \qquad sin\delta_2 = \frac{c\rho(\omega_1 - \omega_3)}{\sqrt{4k_1^2 + c^2\rho^2(\omega_1 - \omega_3)^2}} \tag{5e}$$

$$cos\delta_3 = \frac{2k_1}{\sqrt{4k_1^2 + c^2\rho^2(\omega_2 - \omega_3)^2}}, \qquad sin\delta_3 = \frac{c\rho(\omega_2 - \omega_3)}{\sqrt{4k_1^2 + c^2\rho^2(\omega_2 - \omega_3)^2}}$$

(iv) Sum-sidebands: They are sum-sidebands with sum frequencies of $(\omega_1 + \omega_2)$, $(\omega_1 + \omega_3)$ and $(\omega_2 + \omega_3)$.

$$\frac{8k_2 A_1 A_2 c^2 \rho^2 \omega_1 \omega_2}{\sqrt{4k_1^2 + c^2\rho^2\omega_1^2}\sqrt{4k_1^2 + c^2\rho^2\omega_2^2}\sqrt{4k_1^2 + c^2\rho^2(\omega_1+\omega_2)^2}} sin[(\omega_1 + \omega_2)t - (\theta_1 + \theta_2) + \delta_4] +$$

$$\frac{8k_2 A_1 A_3 c^2 \rho^2 \omega_1 \omega_3}{\sqrt{4k_1^2 + c^2\rho^2\omega_1^2}\sqrt{4k_1^2 + c^2\rho^2\omega_3^2}\sqrt{4k_1^2 + c^2\rho^2(\omega_1+\omega_3)^2}} sin[(\omega_1 + \omega_3)t - (\theta_1 + \theta_3) + \delta_5] +$$

$$\frac{8k_2 A_2 A_3 c^2 \rho^2 \omega_2 \omega_3}{\sqrt{4k_1^2 + c^2\rho^2\omega_2^2}\sqrt{4k_1^2 + c^2\rho^2\omega_3^2}\sqrt{4k_1^2 + c^2\rho^2(\omega_2+\omega_3)^2}} sin[(\omega_2 + \omega_3)t - (\theta_2 + \theta_3) + \delta_6] \tag{5f}$$

$$cos\delta_4 = \frac{c\rho(\omega_1 + \omega_2)}{\sqrt{4k_1^2 + c^2\rho^2(\omega_1 + \omega_2)^2}}, \qquad sin\delta_4 = \frac{2k_1}{\sqrt{4k_1^2 + c^2\rho^2(\omega_1 + \omega_2)^2}} \tag{5g}$$

$$cos\delta_5 = \frac{c\rho(\omega_1 + \omega_3)}{\sqrt{4k_1^2 + c^2\rho^2(\omega_1 + \omega_3)^2}}, \qquad sin\delta_5 = \frac{2k_1}{\sqrt{4k_1^2 + c^2\rho^2(\omega_1 + \omega_3)^2}}$$

$$cos\delta_6 = \frac{c\rho(\omega_2 + \omega_3)}{\sqrt{4k_1^2 + c^2\rho^2(\omega_2 + \omega_3)^2}}, \qquad sin\delta_6 = \frac{2k_1}{\sqrt{4k_1^2 + c^2\rho^2(\omega_2 + \omega_3)^2}}$$

Combining DC component, second-order harmonics and sidebands of Eq.(5) to obtain expression of $\xi_2(t)$, and then from Eq.(6) the transmitted wave is found,

$$u_T(\psi) = \frac{K_2}{K_1}\sum_{i=1}^{3}\frac{A_i^2 c^2\rho^2\omega_i^2}{4k_1^2+c^2\rho^2\omega_i^2} + \sum_{i=1}^{3}\frac{A_i c\rho\omega_i}{\sqrt{4k_1^2+c^2\rho^2\omega_i^2}}cos(\omega_i\psi - \theta_i) +$$

$$\sum_{i=1}^{3}\frac{2k_2 A_i^2 c^2\rho^2\omega_i^2}{\sqrt{k_1^2+c^2\rho^2\omega_i^2(4k_1^2+c^2\rho^2\omega_i^2)}}cos(2\omega_i\psi - 2\theta_i - \xi_i) -$$

$$\frac{8k_2 A_1 A_2 c^2\rho^2\omega_1\omega_2}{\sqrt{4k_1^2+c^2\rho^2\omega_1^2}\sqrt{4k_1^2+c^2\rho^2\omega_2^2}\sqrt{4k_1^2+c^2\rho^2(\omega_1-\omega_2)^2}}cos[(\omega_1-\omega_2)\psi - (\theta_1-\theta_2) - \delta_1] -$$

$$\frac{8k_2 A_1 A_3 c^2\rho^2\omega_1\omega_3}{\sqrt{4k_1^2+c^2\rho^2\omega_1^2}\sqrt{4k_1^2+c^2\rho^2\omega_3^2}\sqrt{4k_1^2+c^2\rho^2(\omega_1-\omega_3)^2}}cos[(\omega_1-\omega_3)\psi - (\theta_1-\theta_3) - \delta_2] -$$

$$\frac{8k_2 A_2 A_3 c^2\rho^2\omega_2\omega_3}{\sqrt{4k_1^2+c^2\rho^2\omega_2^2}\sqrt{4k_1^2+c^2\rho^2\omega_3^2}\sqrt{4k_1^2+c^2\rho^2(\omega_2-\omega_3)^2}}cos[(\omega_2-\omega_3)\psi - (\theta_2-\theta_3) - \delta_3] +$$

$$\frac{8k_2 A_1 A_2 c^2\rho^2\omega_1\omega_2}{\sqrt{4k_1^2+c^2\rho^2\omega_1^2}\sqrt{4k_1^2+c^2\rho^2\omega_2^2}\sqrt{4k_1^2+c^2\rho^2(\omega_1+\omega_2)^2}}sin[(\omega_1+\omega_2)\psi - (\theta_1+\theta_2) + \delta_4] +$$

$$\frac{8k_2 A_1 A_3 c^2\rho^2\omega_1\omega_3}{\sqrt{4k_1^2+c^2\rho^2\omega_1^2}\sqrt{4k_1^2+c^2\rho^2\omega_3^2}\sqrt{4k_1^2+c^2\rho^2(\omega_1+\omega_3)^2}}sin[(\omega_1+\omega_3)\psi - (\theta_1+\theta_3) + \delta_5] +$$

$$\frac{8k_2 A_2 A_3 c^2\rho^2\omega_2\omega_3}{\sqrt{4k_1^2+c^2\rho^2\omega_2^2}\sqrt{4k_1^2+c^2\rho^2\omega_3^2}\sqrt{4k_1^2+c^2\rho^2(\omega_2+\omega_3)^2}}sin[(\omega_2+\omega_3)\psi - (\theta_2+\theta_3) + \delta_6] \qquad (6)$$

where $\psi = x - ct$. The acoustic distortion of sidebands in the transmitted wave is taken as the measurements in this study [33].

Cross-modulation effect takes place when two waves, namely low-frequency pump wave and high-frequency carrier wave, propagate in damage medium. In order to have clear labels to easily figure out the high frequency and low frequencies, the f_H represents high-frequency f_1 of the carrier wave. f_2 and f_3 of the low-frequency pump wave are transferred into f_{L1} and f_{L2} ($f_{L1} < f_{L2}$), respectively. In damage medium, sidebands occur at the frequencies of $f_H \pm nf_{L1}$, $f_H \pm nf_{L2}$ and $f_1 \pm nf_{L2} \pm nf_{L1}$ (where n = 1,2,3 …) as shown in Fig.2. In this study, interactions between f_{L1} and f_{L2} are omitted. Because f_{L1} and f_{L2} are not both frequencies of pump wave in which wavelengths are much larger than the size of flaws;

hence interaction between these two frequencies do not contain much more information about defects and cracks. Sidebands at $f_H \pm nf_{L1}$ are not included in the nonlinear parameter because sidebands at $f_H \pm nf_{L1}$ from these experimental results are close to f_H to be easily masked by carrier wave component. With the damage accumulation, part of energy shifts to sidebands to make their amplitudes increase, and hence, the amplitude of sidebands can be measured as a damaged indicator. A nonlinear parameter D_α can obtained from the relationship in Eq. (8):

$$D_\alpha \sim \frac{\sum A_{H \pm L2} + \sum A_{H \pm L2 \pm L1}}{A_H A_{L2}} \tag{7}$$

where $\sum A_{H \pm L2}$ and $\sum A_{H \pm L2 \pm L1}$ are the sum of sideband amplitude at frequencies of $f_H \pm nf_{L2}$ and $f_H \pm nf_{L2} \pm nf_{L1}$, respectively. A_H and A_{L2} is the spectral amplitude of carried wave and dominant pump frequency, respectively. f_{L2} is usually observed in experiments to be dominant pump frequency.
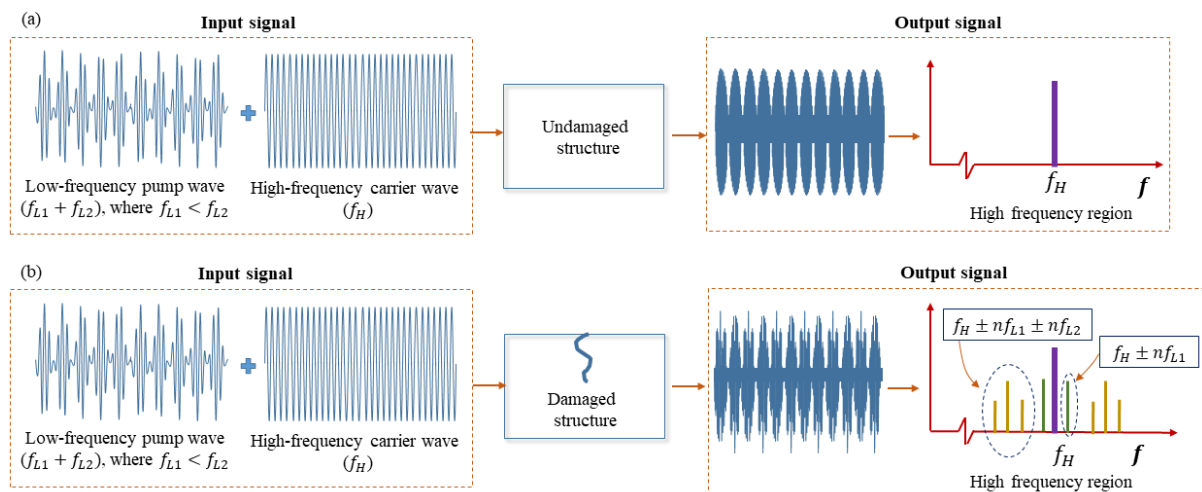

Fig.2 Schematic diagram of the CMVA technique: (a) undamaged structure, (b) damaged structure.

3. Specimen preparation and damage generation

3.1 Specimens

The UHP-FRC was prepared using the sulphate resisting cement, silica fume, sand and steel fibre. The 28-day compressive strength of sulphate resisting cement is 60MPa. The bulk density of the uncondensed silica fume is 635kg/m^3 and silicon dioxide (SiO_2) content is over 89.6%. They were used as mineral admixture. Natural washed river sand, with the maximum nominal

particle size of 4mm was used as fine aggregate. A polycarboxylic ether based superplasticizer was added into the mix to achieve a better workability for UHP-FRC. Straight and hooked steel fibres with the aspect ratio of 0.65 were added into mix as micro and macro fibre. The detailed properties of these two types of fibre are listed in Table 1. The proportions of the various ingredients of UHP-FRC in this study are shown in Table 2. Four UHP-FRC specimens (100mm×100mm×500mm) were cured in a standard curing environment (23°C and 95% relative humidity) for 90 days after demolding, and they were labelled as A1, A2, B1 and B2, respectively.

Table 1 Properties of fibres

Type of fibre	Diameter (mm)	Length (mm)	Aspect ratio	Tensile strength (MPa)	Young's modulus (GPa)
Micro fibres: Straight	0.20	13	0.65	2850	210
Hook end Dramix 3D-65/35 BG	0.55	35	0.65	1345	210

Table 2 Mix proportion of the UHP-FRC specimens

Ingredients	Type	Weight ratio
Cement	Sulphate resisting	1.000
Silica Fume	Uncondensed	0.266
Sand	Natural washed river sand	1.000
Water	-	0.165
Superplasticizer	Polycarboxylic ether based	0.038
Micro fibre	Micro fibres: Straight	0.155
Macro fibre	Hook end Dramix 3D-65/35 BG	0.052

3.2 Three-point flexural test

There are two groups of specimens in this study. The first group of UHP-FRC specimens (labelled as A-series) was loaded directly without pre-treatment. The specimen A1 and A2 were the same. For the other group of UHP-FRC specimens (labelled as B-series), a notch was artificially created at mid-length of specimens before flexural test. The sizes of the notches in specimens B1 and B2 are 7mm×2mm, and 7mm×4mm (width×depth), respectively. A universal testing machine was used and the loading rate was 0.4mm/min. The testing machine was stopped when the loading applied on the specimens reached 30kN. The specimens were then taken out for evaluation using the proposed CMVA technique and standard dynamic elastic modulus test. This loading process was repeated three times. After three loading cycles, the specimen was loaded beyond 30kN until it reaches its ultimate flexural strength. Different levels of damage were induced the UHP-FRC specimens in these loading processes. From the intact state to final loading state, there are five states designated as intact state, state 1, state 2, state 3 and state 4, respectively. A camera with microscope control mode and LED light was

used as crack detector to record the surface cracks created on these UHP-FRC specimens. The growth of cracks is shown in Fig.3.

The flexural strength of UHP-FRC specimen is obtain by Eq. (8) [34].

$$\sigma_b = \frac{3P_{max}L}{2b(h - a_0)^2} \tag{8}$$

where P_{max} is the maximum load; b and h are width and height of specimens, respectively. a_0 is notch depth, and L is the span length. It should be noted that specimens marked A- presents the specimen without notch whereas the B- specimens were introduced notches. To better explore the effect of notch with different depth, B1 and B2 refer to specimen with notch depth of 2mm and 4mm, respectively. Additionally, the flexural strength of UHP-FRC specimens were showed in Table.3.

Table 3 Flexural strength of UHP-FRC specimens

Specimen	L (mm)	b (mm)	h (mm)	a_0 (mm)	P_{max} (kN)	σ_b (MPa)
A1				-	49.88	26.94
A2	360	100	100	-	34.28	21.46
B1				2	38.16	23.44
B2				4	40.01	18.51

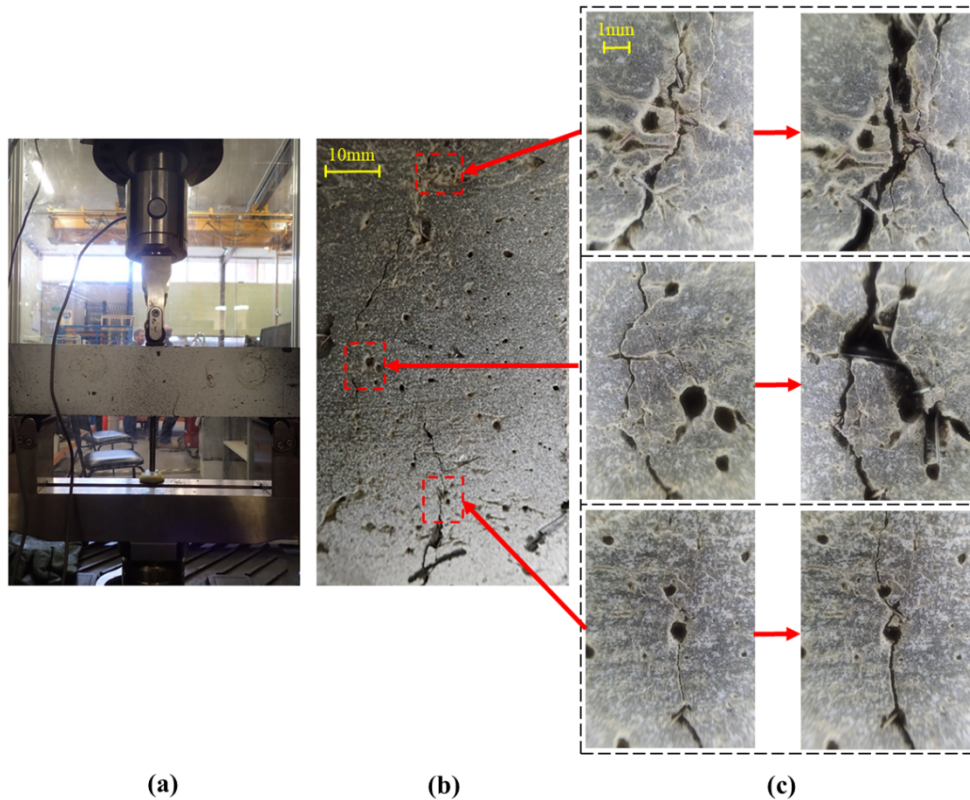(a)   (b)   (c)

Fig.3 Cracks of specimen B2 under different levels of loadings, (a) flexural test in progress; (b) bottom surface of the specimen; (c) growth of cracks from state 3 (on the left side) to state 4 (on the right side)

4. Experimental procedure and signal processing

4.1 Selection of modulated pump wave frequencies for the proposed CMVA technique

To maximize the interaction between vibro-acoustic wave and cracks, experimental modal analysis was performed to obtain the resonant frequencies of UHP-FRC. Then f_{L1} and f_{L2} were selected from resonant response in frequency domain according to the amplitudes. Although frequency responses slightly shifted when the damage was accumulated, these two selected frequencies were still applied throughout entire evaluation using the improved CMVA technique. Firstly, modulation effect was not obvious at early states, particularly at intact state, therefore these frequencies were selected at intact state to ensure adequate modulated interaction by exciting structural response with large enough magnitude. Secondly, modulation effect was evident by observing the increasing amplitude of sidebands at later damage states. Although the selected frequencies were not structural resonance frequencies, which have frequency shifts caused by the damage, excitation of structural response was still sufficient. The selected frequencies were the same for all improved CMVA tests for the purpose of controlling experimental variables and allow comparison of the results. In addition, it is laborious to obtain exact structural resonances from field measurements, so the arbitrary frequency selection is more practical for real applications. These two selected frequencies indirectly demonstrate that arbitrary frequency selection can ensure the improved CMVA technique have good performance.

It should be noted that the locations of struck and accelerometer in this test are different from the standard resonant frequency test in Section 4.3. In this test, to find the two frequencies of the pump wave of the improved CMVA technique, the location of the accelerometer is the same as receiving transducer used in improved CMVA experiments. The location of the struck is also at the same position as the electromagnetic vibration exciter set-up in the improved CMVA experiments. The frequency response of specimen A1 is shown in Fig.4. There are four vibration modes at 243.1Hz, 428.8Hz, 821.2Hz and 1007Hz, respectively. In this study, 240Hz and 1000Hz were selected as frequencies of modulated pump wave for the following reasons:

- It has better control of the resonance vibration. When the electromagnetic vibration shaker emits signal with frequency the same with structural resonance response, it induces intensive vibration. However, intensive vibration affects robustness of contact condition between transducers and specimens. Therefore, the frequency responses with appropriate amplitude are chosen in this study. The amplitudes at 243.1Hz and 1007Hz

are close to 0.018 and they are more suitable compared to the large amplitudes at 428.8Hz and 821.2Hz.

- The difference between f_{L1} and f_{L2} should be large enough, otherwise, sidebands are masked by each other. Therefore, 243.1Hz and 1007Hz were chosen in this study because the difference between 243.1Hz and 1007Hz is larger than the difference between any other two frequency responses.

- It is effective to reduce the resolution requirement. The frequency resolution is defined as $\Delta f = f_s/N$, where f_s is sampling frequency and N is number of data points. If selected frequencies are kept on one decimal place, then Δf should also be accurate to one decimal point by decreasing sampling frequency. Thus, instruments with high-resolution are required and it is possible to prevent further application of CMVA technique. Hence, 243.1Hz and 1007Hz are simplified into 240Hz and 1000Hz, respectively.
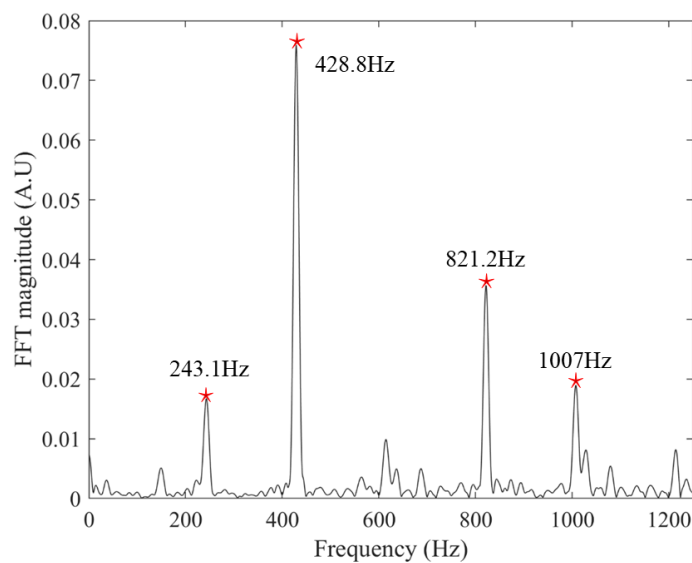

Fig.4 Frequency response for specimen A1

4.2 Experimental set-up of the proposed CMVA technique

The experimental set-up of the proposed CMVA technique is shown in Fig.5. A modulated continuous sinusoidal signal with frequency of 1kHz and 240Hz was first generated by signal generator and used as low-frequency pump wave. It was then fed into a power amplifier before feeding into electromagnetic vibration exciter. To suppress attenuation of ultrasonic wave propagating in UHP-FRC, 50kHz was selected as frequency of carrier wave. Thus, a continuous sinusoidal signal at 50kHz was generated by a function generator and then

transmitted into an emitting transducer. The peak-to-peak voltage of the pump wave remains the same during the experiments while the peak-to-peak voltage of the carried wave was progressive increasing with a steady rate. A total of ten voltage levels were used to calculate one nonlinear parameter, and this procedure was repeated three times to avoid measurement errors in the experiment. Pump wave and carrier wave propagate in UHP-FRC specimens and were captured by the receiving transducer. The signal modulated by pump wave and carried wave was recorded by digitizer for further signal processing and analysis. Two transducers were coupled with UHP-FRC specimens using vacuum grease to ensure a smooth and robust contact between the transducers and specimens. Additionally, the electromagnetic exciter and emitting transducer were located at a distance of 50 mm and 70 mm from one end of the specimens, respectively. While the other receiving transducer was located at 50 mm from the other side of the specimens.
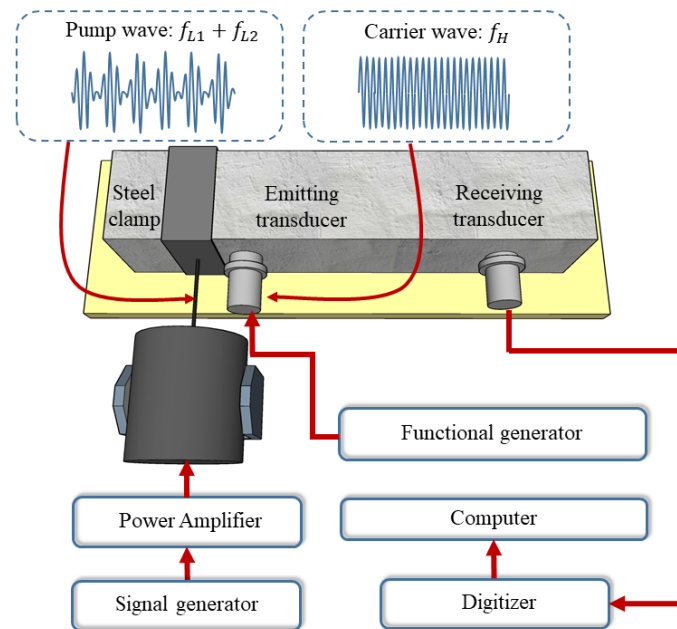

Fig.5 Experimental set-up of the proposed CMVA technique

4.3 The dynamic Young's modulus of elasticity E_d

To further characterize the damage levels of the UHP-FRC specimens and compare the results of the improved CMVA technique with the conventional dynamic elastic modulus tests using the impact resonance method shown in ASTM C215-02. Ten measurements of longitudinal resonant frequency were obtained at each damage stage for each specimen and the averaged values were calculated.

4.4 Extraction of Nonlinear parameter

The measured time domain signal and frequency spectrum of specimen A2 are shown in Fig. 6. Fast Fourier transform (FFT) was used to transform the signal from time domain into frequency domain. Fig.6 shows that sidebands mainly appear at frequencies of (50kHz ± n×1kHz) and 50kHz ± (n×1kHz ± m×0.24kHz), and the prominent amplitudes were obtained in first and second order sidebands (n=1, 2, and m=1). Some other higher order sidebands were omitted when calculating nonlinear parameters of the imrpoved CMVA technique in this study, including the sidebands at (50kHz ± m×0.24kHz) because they are too close to the main high-frequency component at 50kHz, which can be easily masked. Finally, the sidebands at 47.76kHz, 48kHz, 48.24kHz, 48.76kHz, 49kHz, 49.24kHz, 50.76kHz, 51kHz, 51.24kHz, 51.76kHz, 52kHz and 52.24kHz were used in the calculation of $\sum A_s$.

According to Equation (8), nonlinear parameter D_α is defined as the slope of data points ($\sum A_s$, $A_H A_{L2}$) under ten peak-to-peak voltage levels. Fig.7 shows a linear relationship of $\sum A_s$ and $A_H A_{L2}$ for the specimen A1 under five different damage levels, with high coefficients of determination ($R^2 \geq 0.95$).
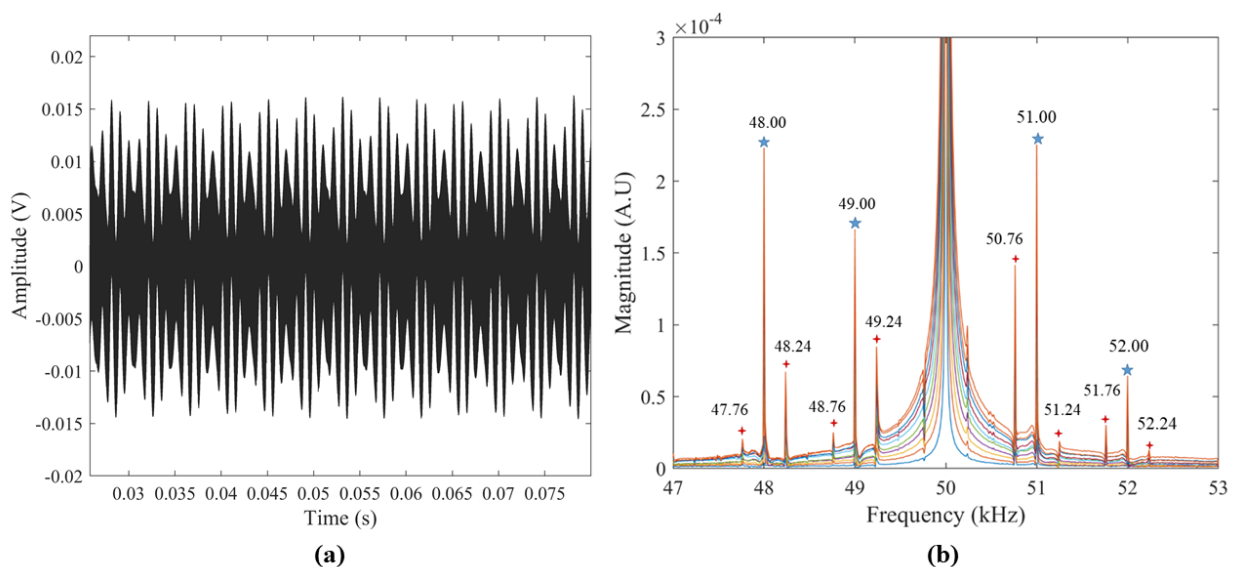

Fig.6 Typical signal of modulation wave: (a) time domain; (b) frequency domain.
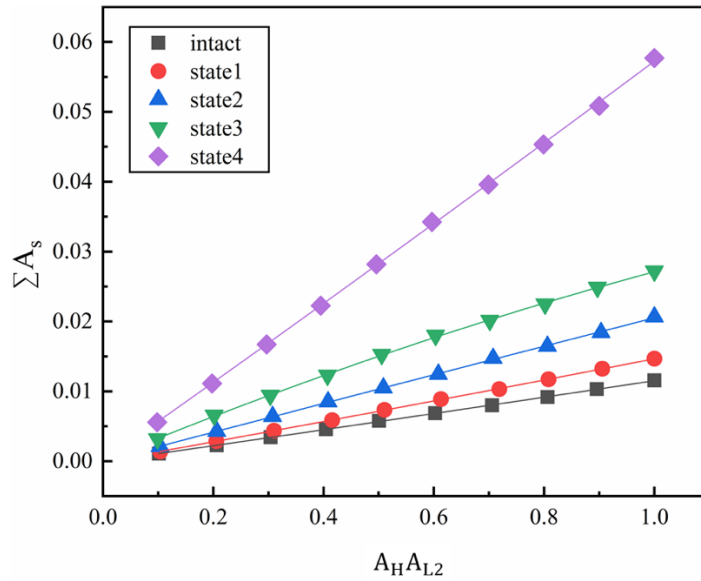
Fig.7 Nonlinear parameter of specimen B2 in different state (Linear relationship of $A_H A_{L2}$ and $\sum A_s$).

5. Results and discussions

5.1 Results of fundamental longitudinal resonant frequencies

The elastic modulus has been widely used as indicator in conventional techniques to characterize defects in structures. In this study, the fundamental longitudinal resonant frequencies of the four specimens at five different states were measured for calculating dynamic Young's modulus of elasticity. The results are shown in Fig.8, where the maximum magnitudes are normalized to allow direct comparison. The fundamental longitudinal resonant frequencies are slightly shifted toward to low frequency. The largest shift happens between state 3 to state 4 because the specimens were loaded to its ultimate damage strength instead of applying a steady loading step of 30kN. It should be noted that the frequency domain of specimen B2 is slightly different to the other three specimens because the coupling mode occurred. Besides of resonant frequency response, there was another distinguish frequency components, and these extra responses were caused by coupling mode. It sometimes happens when the structures have evident cracks. Specimen B2 has the largest depth of notch. The cracks of this specimen were obvious after loading test. This coupling mode causes a serious issue. When the damage grows with the loading cycle, more energy is transferred from the fundamental resonant mode to the coupling mode. When the damage reaches certain level, it is difficult to identify the fundamental resonant vibration mode from coupling mode based on the magnitude. Thus, the conventional dynamic elastic modulus test is not reliable and robust due to the coupling effect.
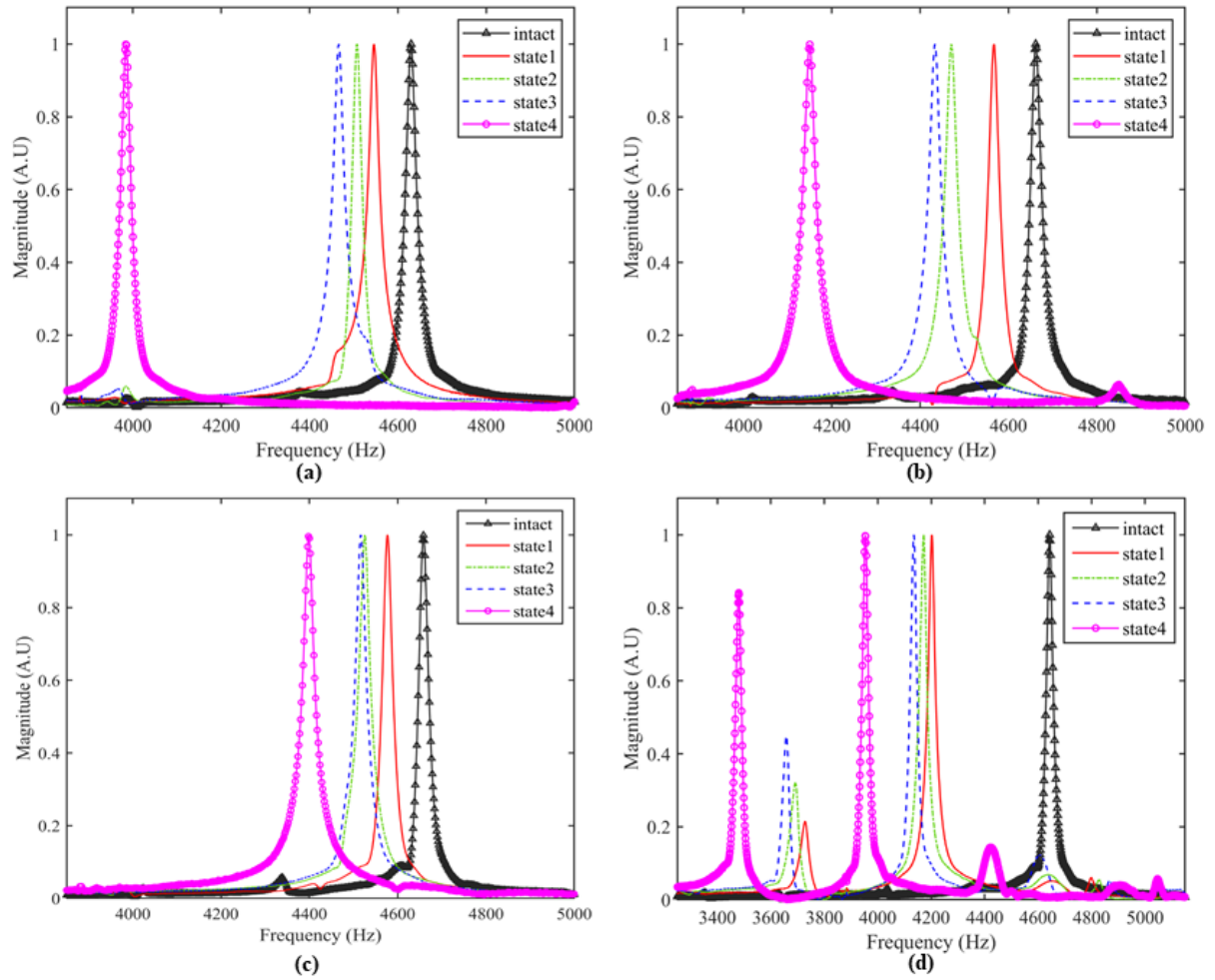
Fig.8 Fundamental longitudinal frequencies at different damage level: (a) specimen A1; (b) specimen A2; (c) specimen B1; (d) specimen B2.

5.2 Results of dynamic elastic modulus test

After obtaining fundamental longitudinal frequency, the dynamic elastic modulus E_d can be calculated using Eq. (9):

$$E_d = 4\frac{L'}{bh}Mf_l{}^2 \tag{9}$$

where L', b and h are length, width and height of specimens, respectively. M is mass and f_l is fundamental longitudinal frequency. The results of E_d for specimen A1, A2, B1 and B2 at different state are shown in Fig.9. The initial value of E_d for these four specimens are different at intact state. In terms of magnitude of resonant frequency, the ranking for the value E_d from largest to smallest within the set of specimens is presented as A2, B1, A1 and B2. This order for the values of E_d differs completely when compared to the order from largest to smallest for the values of σ_b within the same set of specimens. The initial value of E_d indirectly reflects the

flexural properties of specimens, therefore, it indicates that E_d is not very reliable, to some extent, to assess the mechanical properties of UHP-FRC structures according to these experimental results.

Figs. 9(a) and 9(b) show the results of A-series specimens and the results of these two groups of specimens exhibit almost the same trend of decrease. For specimen A1, the relative percentage change from state 1 to state 4 is about 3.60%, 6.61%, 9.69% and 27.16%, respectively. Meanwhile, relative change ratios are 4.02%, 9.38%, 10.88% and 22.02% for the four different damage states of specimen A2, respectively. The trends of E_d of A-series specimens are only slightly decreasing, which indicates the conventional dynamic elastic modulus test is not very sensitive for crack formation and grow.

Figs. 9(c) and 9(d) show the results of E_d for B-series specimens. The value of E_d for specimens B1 and B2 decrease with accumulation of damage in different states. This group of specimens have a notch at mid-span of the specimens to control the formation of the cracks, such as location and type. It is expected that the concentrated cracks initially occur at the middle of bottom surface in B-series specimens, whereas distributed small cracks appear at the locations of two supports in A-series specimens. However, the decreasing trend of the results of specimen B1 is similar to that of A-series specimens. The possible reason is that the size of notch (100mm length×7mm width×2mm depth) of specimen B1 is not large enough. Relative percentage changes for specimen B1 are 3.58%, 5.73%, 6.10% and 12.15%, respectively. The formation of crack in specimen B2 is expected where a small visual crack initially appeared in the middle of bottom surface, and gradually developed as a large dominant crack. The percentage change from intact state to state 1 of specimen B2 is about 18.08% and this is quite large compared with the other three specimens. It is believed that this is caused by the support conditions of the specimens (see ASTM C215-02 Fig.3 (b)) and the size of notch.

According to the analysis of E_d of four UHP-FRC specimens at different states, it is found that the conventional dynamic elastic modulus test is insensitive to characterize evolution of cracks. Furthermore, it is not easy to clearly identify resonant frequency when coupling modes occur. In addition, robustness and consistency of this dynamic elastic modulus test are frequently affected by support conditions and geometry of specimens.
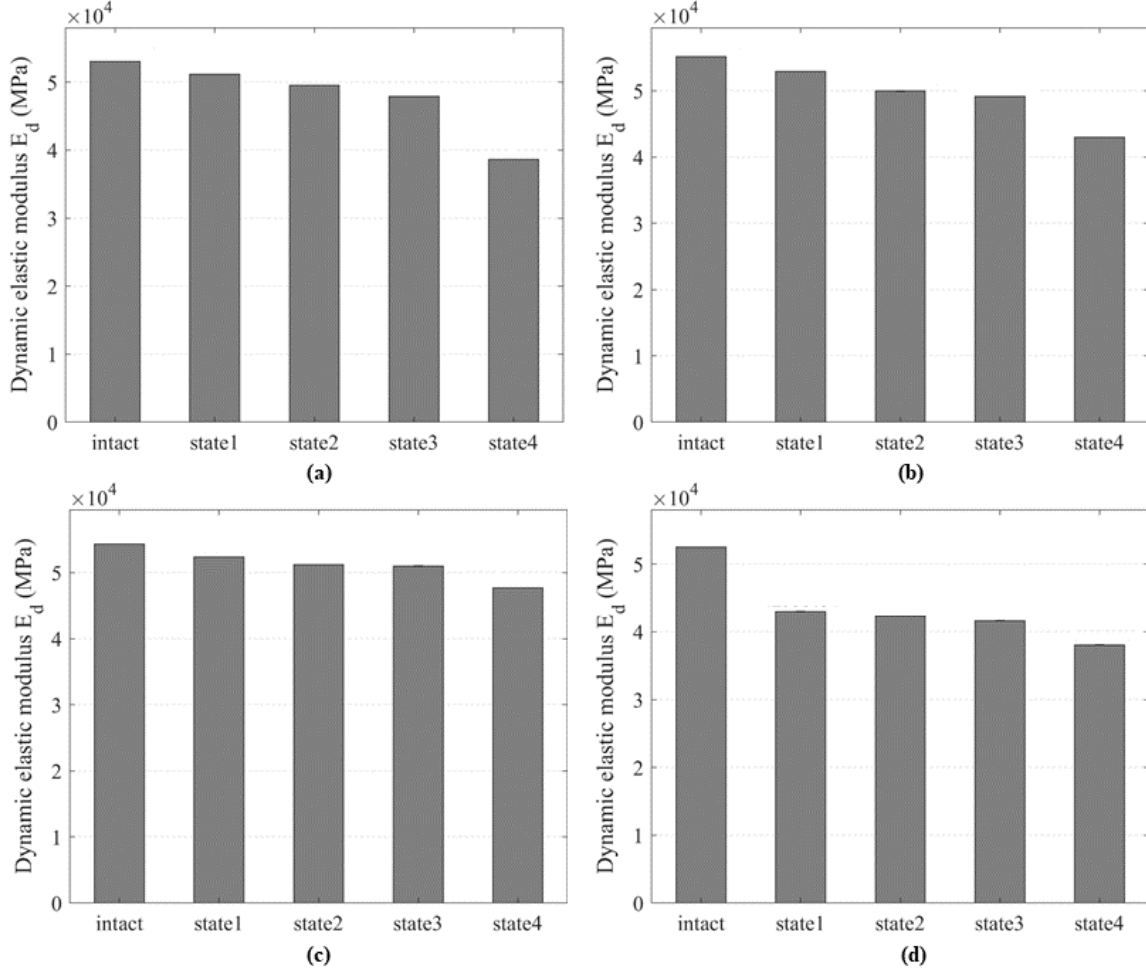
Fig.9 Dynamic elastic modulus: (a) specimen A1; (b) specimen A2; (c) specimen B1; (d) specimen B2.

5.3 Results of the proposed CMVA technique

In this section, the results of the proposed CMVA technique, 1) typical frequency domain at five different states, and 2) nonlinear parameter D_α, are presented. Fig.10 shows the frequency domain data of specimen B2 at state 1, state 2, state 3 and state 4, respectively. The sidebands shown in Fig.10(a) for state 1 mainly occur at the frequency of $(50\pm n\times 1)$kHz, i.e. 48kHz, 49kHz, 51kHz, and 52kHz. The amplitudes of these sidebands are small. At state 2, as shown in Fig.10(b), sidebands at frequencies $(50\pm n\times 1)$kHz still play a dominant role and the magnitudes slightly increase.

There are some other sidebands at the frequencies of $50 \pm (n\times 1 \pm m\times 0.24)$kHz, such as 47.76kHz, 48.24kHz, 48.76kHz, 49.24kHz, 50.76kHz, 41.24kHz, 51.76kHz, 52.24kHz. In Fig. 10(c), the magnitudes of the sidebands at $(50\pm n\times 1)$kHz and $50\pm(n\times 1 \pm m\times 0.24)$kHz generally increase. Fig. 10(d) shows that, in state 4, the number and the magnitudes of the sidebands increase evidently. Some higher order sidebands, where $n\geq 3$, $m\geq 2$, occur in frequency domain

and the magnitude of these sidebands increase obviously. As mentioned in Section 4.4, the sidebands at specified frequencies are considered in the calculation of nonlinear parameter. Even though some sidebands are ignored, the nonlinear parameter still has high sensitivity in characterizing different levels of damage.
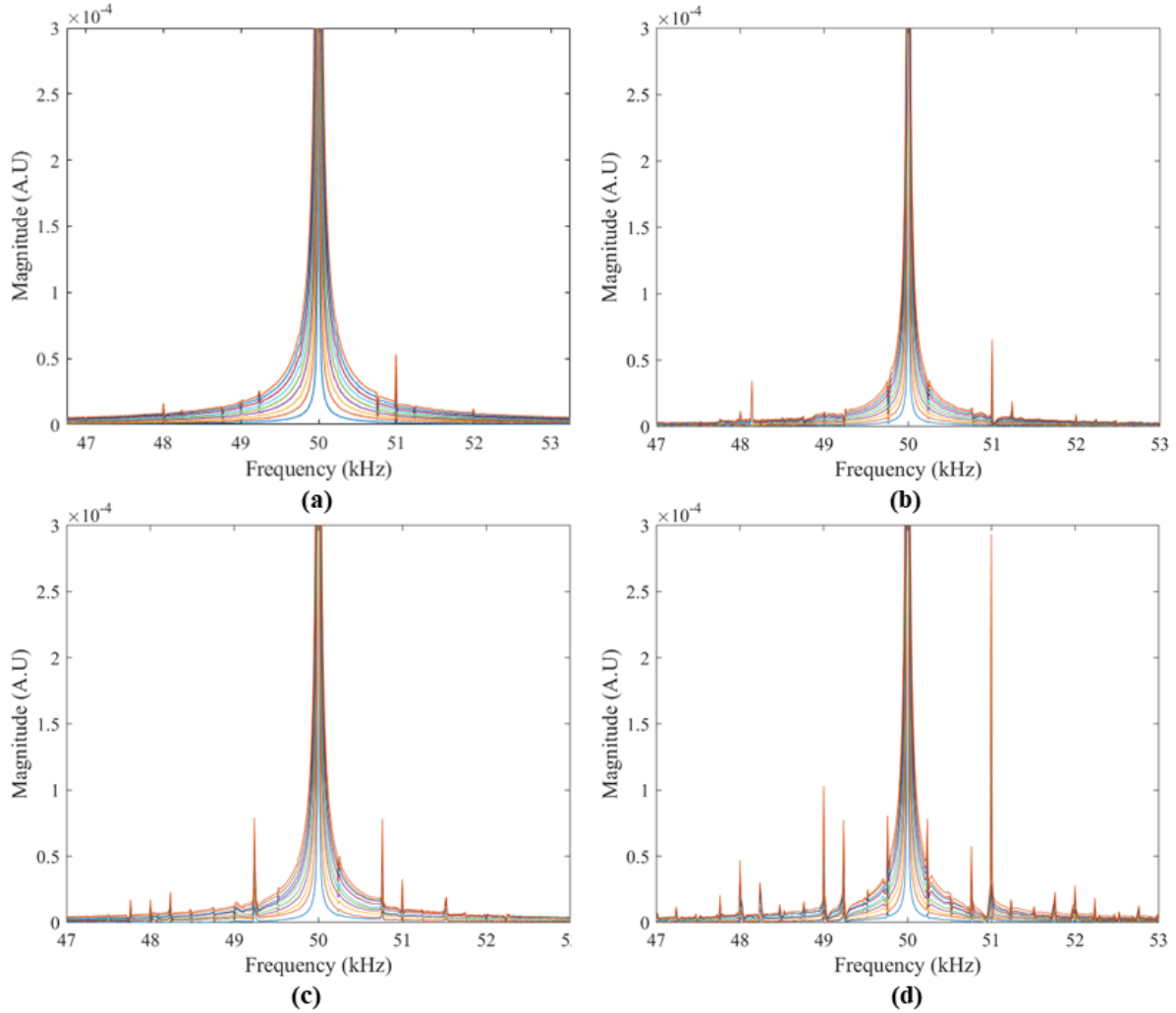

Fig.10 Frequency domain signal for specimen B2: (a) state1; (b) state2; (c) state3; (d) state4.

Nonlinear parameters D_α are calculated using Eq. (7) and presented with error bar in Fig.11. It is observed that nonlinear parameters of these four UHP-RFC specimens at intact state are not zero because of the inherent defects caused during casting and curing procedure. Therefore, the nonlinear parameter D_α can be used to identify not only crack-induced damage, but also material nonlinearity. Formation of inherent defects is unavoidable, and the inherent defects are slightly different even in the same batch of specimens made by the same materials and production process. These inherent defects reduce the mechanical strength of the specimens to some extent. Among the initial nonlinear parameters D_α of these four specimens,

the minimum value of D_α is 0.0096 (specimen A1), followed by 0.0104 (specimen A2), 0.0106 (specimen B1), and 0.0108 (specimen B2). The order of these nonlinear parameters is similar to that of σ_b, which reveals that the nonlinear parameter D_α is a feasible calibre for qualitative assessment of initial state of materials, and provide implication of mechanical strength of the specimens.

Fig.11 shows that the nonlinear parameters present a rapid growth with the accumulation of damage. From intact state to state 1, the nonlinear parameter D_α increases about 50% for specimen A1 and 63% for specimen A2, whereas it increases about 25% and 28% for specimen B1 and specimen B2, respectively. In comparison with B-series specimens, A-series specimens have more growth after first loading cycle. It is because A-series specimens without pre-treatment of notch have some small distributed cracks at two supporting points at the beginning, and the contribution of distributed cracks appeared in multiple areas is more evident than single concentrated crack occurred at one position. Furthermore, it is observed that the geometric change of notch almost has no influence on the nonlinear parameter because the nonlinear parameter does not have a significant growth for B-series specimens from the intact state to the state 1. These experimental results demonstrate the excellent ability of nonlinear parameter in characterizing damage because it only reflects the internal changes of the specimens and is not affected by geometric changes, such as boundary conditions. Moreover, the initial nonlinear parameter D_α of specimen B1 is larger than that of specimen B2. This variation is reasonable because the notch of specimen B1 is small, therefore, its damage accumulation progress is similar to A-series specimens.

Based on the results, the increasing trend of nonlinear parameter D_α is obviously shown in Fig.11. Considering the A-series specimens, the relative change ratios of specimen A1 from state 1 to state 4 are about 50.00%, 110.42%, 212.85% and 330.56%, respectively. For specimen A2, the relative change ratios are 63.02%, 107.72%, 199.39% and 422.96% for state 1 to state 4. In the result of A-series specimens, the minimum increase of D_α is 50%, which is larger than the maximal increase of E_d (about 27.16%) in the final state. Fig.11(a) and 11(b) show the nonlinear parameters D_α of B-series specimens. The increase of D_α for specimen B1 is slightly lower than that of specimen B2, and the overall increase slower compared with specimen B2. Similar trend of E_d is also observed in specimen B1, and the results are related to its damage evolution. The relative change ratios from state 1 to state 4 are still substantial for specimen B2, and they are 24.76%, 76.03%, 124.54% and 198.52%, respectively. D_α of

specimen B2 has a trend of rapid growth, and relative change ratio from state 1 to state 4 is 28.00%, 86.77%, 139.69% and 410.46%, respectively.

The results of initial D_α indicate that the improved CMVA technique is capable to characterize material nonlinearity. Furthermore, these values of nonlinear parameter D_α are consistent regardless of geometric changes caused by the notch. Compared with results of dynamic elastic modulus E_d, the nonlinear parameter D_α has high sensitivity to evolution of the cracks in UHP-FRC materials.
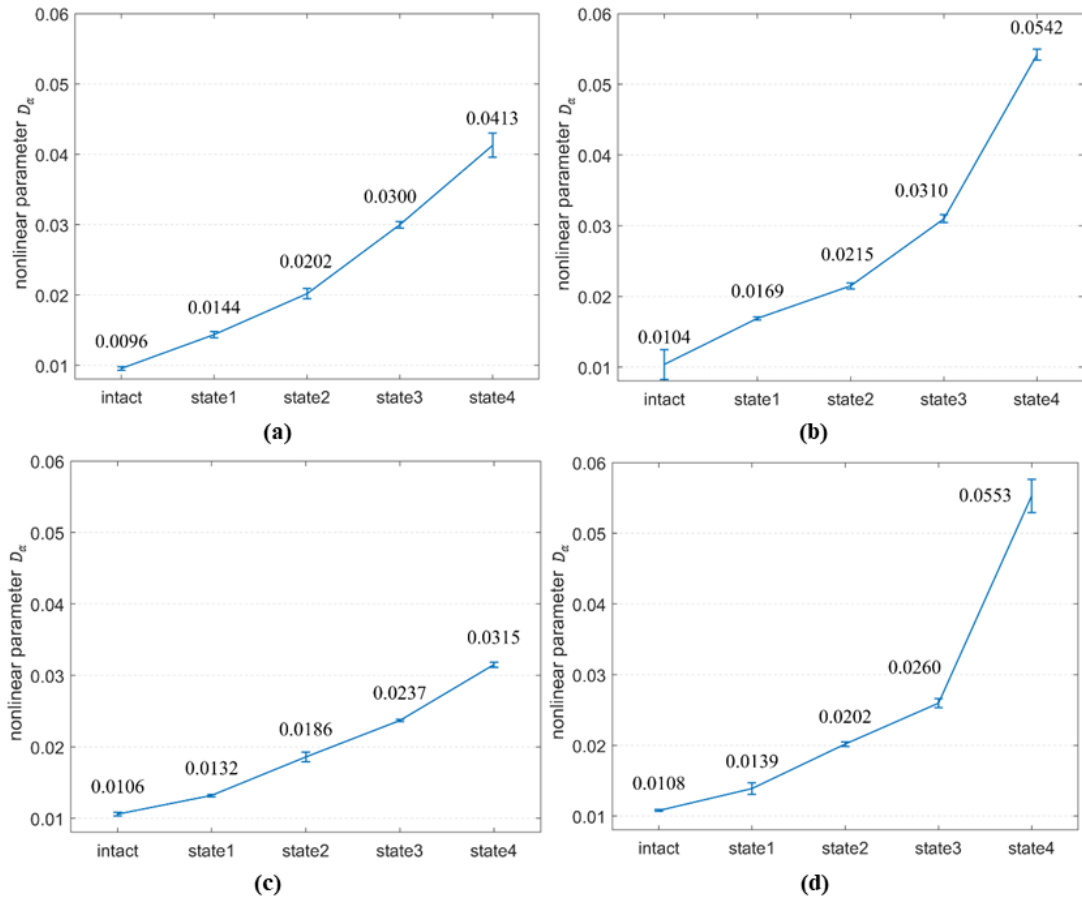

Fig.11 Nonlinear parameter D_α: (a) specimen A1; (b) specimen A2; (c) specimen B1; (d) specimen B2.

5.4 Comparison of nonlinear parameter and dynamic elastic modulus

Along with accumulation of damages, the nonlinear parameter D_α increases while the dynamic elastic modulus E_d decreases. In addition, the unit and order of magnitude are also different. To evaluate and compare the sensitivity of D_α and E_d, dimensionless indexes are defined:

$$\bar{D}_\alpha = |(D_\alpha - D_0)|/D_0 \tag{10}$$

$$\bar{E}_D = |(E_D - E_0)|/E_0 \qquad (11)$$

where E_0 and D_0 correspond to the data at intact state. $\bar{D}_\alpha$ and $\bar{E}_D$ are dimensionless indexes corresponding to the D_α and E_d, respectively, as shown together in Fig.12.

From Fig.12, the variation of $\bar{D}_\alpha$ is 3.306, 4.230, 2.286 and 4.105 corresponding to A1, A2, B1 and B2, respectively. The largest variation of $\bar{E}_D$ is not more than 0.3. Along with the accumulation of damages, the $\bar{D}_\alpha$ has shaper rise than $\bar{E}_D$. In addition, the $\bar{D}_\alpha$ is generally one order of magnitude larger than $\bar{E}_D$. This implies that the improved CMVA technique has a much higher sensitivity to the damages than the conventional approach using the unamic elastic modulus.
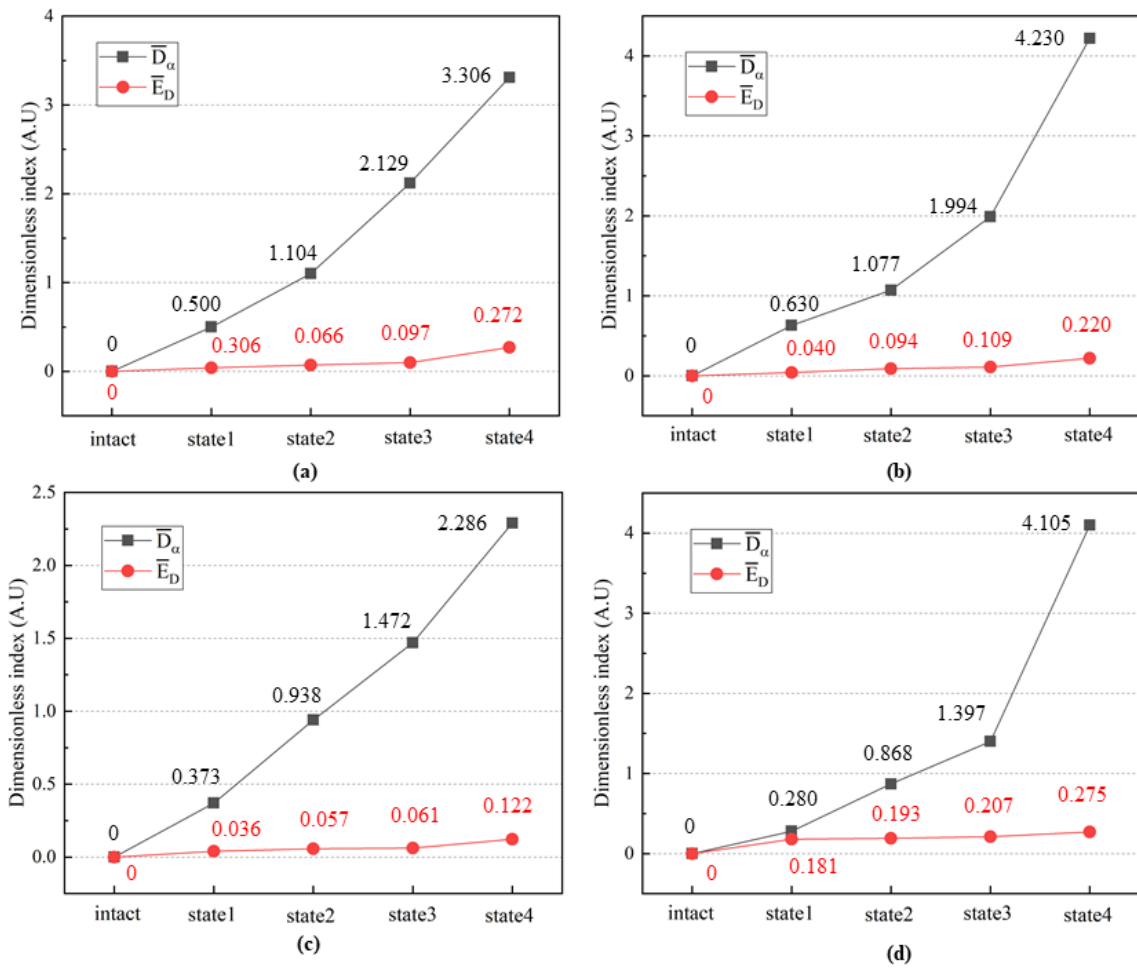

Fig.12 Comparison of $\bar{D}_\alpha$ and $\bar{E}_D$: (a) specimen A1; (b) specimen A2; (c) specimen B1; (d) specimen B2.

6. Conclusions

This study has developed an improved CMVA technique to evaluate the damage evolution in UHP-FRC materials under flexural loading using nonlinear parameter D_α. The results have shown that the improved CMVA technique is feasible for characterizing bending damage and evaluating the damage growth. The improved CMVA technique is based on two independent waves, namely, low-frequency pump wave and high-frequency carrier wave. The technique has advantages of applying modulated pump wave with frequency f_{L1} and f_{L2} to arouse resonance frequency, maintaining robust contact condition between the transducers and specimens, and also avoiding the need of high-power electromagnetic shaker. The cross-modulation effect due to interaction between pump wave and carrier wave could be observed in frequency domain. The number and amplitude of sidebands increase with the accumulation of damage. In this study, the nonlinear parameter D_α has been developed and used as an indicator for evaluating bending damage. The nonlinear parameter D_α increases during the entire course of flexural test, particularly at early damage state.

The improved CMVA technique is reliable compared to conventional ASTM technique. The results of conventional ASTM technique are usually affected by experimental conditions and manufacturing process of samples, and the resonance frequency can be masked by coupling modes. However, the measurement procedure of the improved CMVA technique is robust to be used in field applications. The improved CMVA technique has high sensitivity for detecting cracks in UHP-FRC materials compared to conventional ASTM technique. The nonlinear parameter D_α has a maximum relative change ratio of 422.96%, while the change of dynamic elastic modulus E_d is only about 27.48%.

In this study, the feasibility, reliability and sensitivity of the improved CMVA technique have been validated and demonstrated. With the increasing applications of UHP-FRC materials, the development of damage detection techniques for UHP-FRC material has attracted significant attention. This study has shown that the improved CMVA technique is an effective method for detecting and identifying cracks in UHP-FRC materials, and can be potentially used for field applications.

Acknowledgement

References

1. Guo, Z., *Principles of reinforced concrete*. 2014: Butterworth-Heinemann.
2. Naebe, M., M.M. Abolhasani, H. Khayyam, A. Amini, and B. Fox, *Crack damage in polymers and composites: A review*. Polymer reviews, 2016. **56**(1): p. 31-69.
3. Lacouture, J.-C., P.A. Johnson, and F. Cohen-Tenoudji, *Study of critical behavior in concrete during curing by application of dynamic linear and nonlinear means*. The Journal of the Acoustical Society of America, 2003. **113**(3): p. 1325-1332.
4. Hughes, J.M., M. Mohabuth, A. Khanna, J. Vidler, A. Kotousov, and C.-T. Ng, *Damage detection with the fundamental mode of edge waves*. Structural Health Monitoring, 2021. **20**(1): p. 74-83.
5. Tsioulou, O., A. Lampropoulos, and S. Paschalis, *Combined non-destructive testing (NDT) method for the evaluation of the mechanical characteristics of ultra high performance fibre reinforced concrete (UHPFRC)*. Construction and Building Materials, 2017. **131**: p. 66-77.
6. Nematzadeh, M., M. Tayebi, and H. Samadvand, *Prediction of ultrasonic pulse velocity in steel fiber-reinforced concrete containing nylon granule and natural zeolite after exposure to elevated temperatures*. Construction and Building Materials, 2021. **273**: p. 121958.
7. Treiber, M., J.-Y. Kim, J. Qu, and L.J. Jacobs, *Effects of sand aggregate on ultrasonic attenuation in cement-based materials*. Materials and structures, 2010. **43**(1): p. 1-11.
8. Torello, D., S. Thiele, K.H. Matlack, J.-Y. Kim, J. Qu, and L.J. Jacobs, *Diffraction, attenuation, and source corrections for nonlinear Rayleigh wave ultrasonic measurements*. Ultrasonics, 2015. **56**: p. 417-426.
9. Yang, Y., C.T. Ng, M. Mohabuth, and A. Kotousov, *Finite element prediction of acoustoelastic effect associated with Lamb wave propagation in pre-stressed plates*. Smart Materials and Structures, 2019. **28**(9): p. 095007.
10. Yeung, C. and C.T. Ng, *Nonlinear guided wave mixing in pipes for detection of material nonlinearity*. Journal of Sound and Vibration, 2020. **485**: p. 115541.
11. Eiras, J., T. Kundu, J. Popovics, and J. Payá, *Cement-based material characterization using nonlinear single-impact resonant acoustic spectroscopy (NSIRAS)*, in *Nonlinear Ultrasonic and Vibro-Acoustical Techniques for Nondestructive Evaluation*. 2019, Springer. p. 487-508.
12. Lim, H.J. and H. Sohn, *Online fatigue crack prognosis using nonlinear ultrasonic modulation*. Structural Health Monitoring, 2019. **18**(5-6): p. 1889-1902.
13. Kundu, T., *Nonlinear ultrasonic and vibro-acoustical techniques for nondestructive evaluation*. 2018: Springer.
14. Yang, Y., C.-T. Ng, and A. Kotousov, *Influence of crack opening and incident wave angle on second harmonic generation of Lamb waves*. Smart Materials and Structures, 2018. **27**(5): p. 055013.

15. Yang, Y., C.-T. Ng, and A. Kotousov, *Second harmonic generation of guided wave at crack-induced debonding in FRP-strengthened metallic plates.* International Journal of Structural Stability and Dynamics, 2019. **19**(01): p. 1940006.

16. Chen, J., C. Yang, and Q. Guo, *Evaluation of surface cracks of bending concrete using a fully non-contact air-coupled nonlinear ultrasonic technique.* Materials and Structures, 2018. **51**(4): p. 1-9.

17. Kim, G., G. Loreto, J.-Y. Kim, K.E. Kurtis, J.J. Wall, and L.J. Jacobs, *In situ nonlinear ultrasonic technique for monitoring microcracking in concrete subjected to creep and cyclic loading.* Ultrasonics, 2018. **88**: p. 64-71.

18. Chen, J., C. Huang, C. Yang, T. Yin, and Q. Guo, *Non-linear ultrasonic investigation of interface debonding of steel-concrete composites.* Insight-Non-Destructive Testing and Condition Monitoring, 2018. **60**(3): p. 155-160.

19. Mohseni, H. and C. Ng, *Higher harmonic generation of Rayleigh wave at debondings in FRP-retrofitted concrete structures.* Smart Materials and Structures, 2018. **27**(10): p. 105038.

20. Mohseni, H. and C.-T. Ng, *Rayleigh wave propagation and scattering characteristics at debondings in fibre-reinforced polymer-retrofitted concrete structures.* Structural Health Monitoring, 2019. **18**(1): p. 303-317.

21. Leśnicki, K.J., J.-Y. Kim, K.E. Kurtis, and L.J. Jacobs, *Assessment of alkali–silica reaction damage through quantification of concrete nonlinearity.* Materials and structures, 2013. **46**(3): p. 497-509.

22. Chen, J., R. Bharata, T. Yin, Q. Wang, H. Wang, and T. Zhang, *Assessment of sulfate attack and freeze–thaw cycle damage of cement-based materials by a nonlinear acoustic technique.* Materials and Structures, 2017. **50**(2): p. 105.

23. Carrión, A., V. Genovés, G. Pérez, J. Payá, and J. Gosálbez, *Flipped accumulative non-linear single impact resonance acoustic spectroscopy (FANSIRAS): a novel feature extraction algorithm for global damage assessment.* Journal of Sound and Vibration, 2018. **432**: p. 454-469.

24. Donskoy, D.M. and A.M. Sutin, *Vibro-acoustic modulation nondestructive evaluation technique.* Journal of intelligent material systems and structures, 1998. **9**(9): p. 765-771.

25. Chen, J., A.R. Jayapalan, J.-Y. Kim, K.E. Kurtis, and L.J. Jacobs, *Nonlinear wave modulation spectroscopy method for ultra-accelerated alkali-silica reaction assessment.* ACI Materials Journal, 2009. **106**(4): p. 340.

26. Chen, J., Y. Wu, T. Yin, N. Talebzadeh, and Q. Guo, *Characterization of concentrated and distributed cracks in concrete using a harmonic wave modulation technique.* Materials and Structures, 2018. **51**(1): p. 1-10.

27. Chen, J., Y. Wu, and C. Yang, *Damage assessment of concrete using a non-contact nonlinear wave modulation technique.* NDT & E International, 2019. **106**: p. 1-9.

28. Zaitsev, V., V. Nazarov, V. Gusev, and B. Castagnede, *Novel nonlinear-modulation acoustic technique for crack detection.* NDT & E International, 2006. **39**(3): p. 184-194.

29. Tournat, V., V.Y. Zaitsev, V. Nazarov, V. Gusev, and B. Castagnède, *Experimental study of nonlinear acoustic effects in a granular medium.* Acoustical Physics, 2005. **51**(5): p. 543-553.

30. Aymerich, F. and W. Staszewski, *Experimental study of impact-damage detection in composite laminates using a cross-modulation vibro-acoustic technique.* Structural Health Monitoring, 2010. **9**(6): p. 541-553.

31. Trojniar, T., A. Klepka, L. Pieczonka, and W. Staszewski. *Fatigue crack detection using nonlinear vibro-acoustic cross-modulations based on the Luxemburg-Gorky effect.* in *Health*

Monitoring of Structural and Biological Systems 2014. 2014. International Society for Optics and Photonics.

32. International, A., *ASTM C215-02 Standard Test Method for Fundamental Transverse, Longitudinal, and Torsional Frequencies of Concrete Specimens*. 2002: West Conshohocken, PA.

33. Wang, Y., X. Zhu, H. Hao, and J. Ou, *Spectral element model updating for damage identification using clonal selection algorithm.* Advances in Structural Engineering, 2011. **14**(5): p. 837-856.

34. International, A., *ASTM C78 / C78M-18 Standard Test Method for Flexural Strength of Concrete (Using Simple Beam with Third-Point Loading)*. 2018: West Conshohocken, PA.